LETTER

doi:10.1038/nature25777

A quantized microwave quadrupole insulator with topologically protected corner states

Christopher W. Peterson[1], Wladimir A. Benalcazar[2], Taylor L. Hughes[2] & Gaurav Bahl[3]

The theory of electric polarization in crystals defines the dipole moment of an insulator in terms of a Berry phase (geometric phase) associated with its electronic ground state[1,2]. This concept not only solves the long-standing puzzle of how to calculate dipole moments in crystals, but also explains topological band structures in insulators and superconductors, including the quantum anomalous Hall insulator[3,4] and the quantum spin Hall insulator[5–7], as well as quantized adiabatic pumping processes[8–10]. A recent theoretical study has extended the Berry phase framework to also account for higher electric multipole moments[11], revealing the existence of higher-order topological phases that have not previously been observed. Here we demonstrate experimentally a member of this predicted class of materials—a quantized quadrupole topological insulator—produced using a gigahertz-frequency reconfigurable microwave circuit. We confirm the non-trivial topological phase using spectroscopic measurements and by identifying corner states that result from the bulk topology. In addition, we test the critical prediction that these corner states are protected by the topology of the bulk, and are not due to surface artefacts, by deforming the edges of the crystal lattice from the topological to the trivial regime. Our results provide conclusive evidence of a unique form of robustness against disorder and deformation, which is characteristic of higher-order topological insulators.

The simplest model of a system with a quantized dipole moment is a one-dimensional two-band insulator[12]. Owing to the presence of chiral or inversion symmetries[13,14], this system exhibits quantized fractional edge charges of $\pm e/2$, where e is the electron charge, when its band structure is topological. The fractional edge charges of the quantized dipole insulator are associated with a pair of edge-localized bound states of the Hamiltonian. These edge states have energies that lie within the bulk insulating gap and have been observed in one-dimensional lattices in systems of cold atoms[15,16] and in several metamaterials[17–20]. However, the possible existence of quantized higher multipole moments protected by spatial symmetries in crystalline insulators has remained an outstanding question for the past 25 years. A recent theory addressing this issue[11] proposes a pair of simple electronic two- and three-dimensional lattice models that exhibit the signatures of quantized electric quadrupole and octupole moments, respectively. A two-dimensional insulator with a quantized quadrupole moment $q_{xy} = e/2$ generates edge-localized dipole moments tangent to the edge of the lattice and corner-localized charges, both of magnitude $e/2$ (Fig. 1a). The corner charges are associated with four corner-localized modes that lie in the middle of the energy gap[11,21] (Fig. 1c). Although the edge-localized polarizations arise from the gapped, but topological, nature of the edge states, they do not have a spectroscopic manifestation.

Metamaterial analogues of quantum Hall and quantum spin Hall topological insulators have previously been implemented in photonic[22–24] and phononic[25,26] systems, as well as in electric circuits[27]. Here, we implement the two-dimensional quadrupole topological model from ref. 11. (Fig. 1b) in a metamaterial composed of coupled microwave resonators. Although edge polarizations and corner-localized, topologically protected modes are both signatures of the

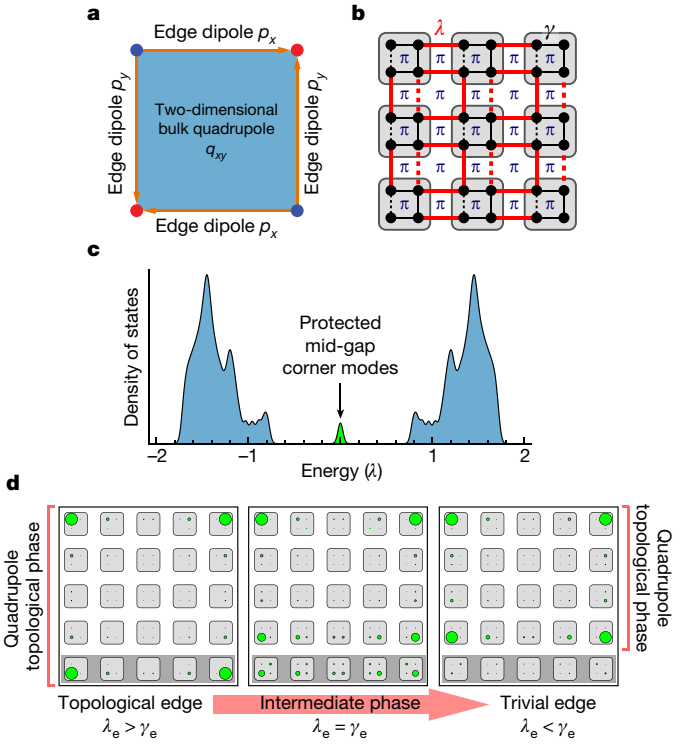

Figure 1 | Quadrupole topological insulator. a, Two-dimensional bulk quadrupole topological insulator (blue square) with edge-localized topological dipoles (orange arrows) and corner-localized charges of $\pm e/2$ (red and blue dots). **b**, Tight-binding representation of a quadrupole topological insulator with four sites per unit cell. Red lines denote coupling between unit cells (coupling rate, λ) and black lines represent couplings within unit cells (γ). Dashed lines indicate a -1 phase factor on the coupling, a gauge choice for the creation of a synthetic magnetic flux of π per plaquette. The insulator is in the quadrupole topological phase for $\lambda > \gamma$ and in the trivial phase for $\lambda < \gamma$. **c**, Theoretically calculated density of states for the quantized quadrupole insulator (5×5 unit cells) shown in **b** with fully open boundaries. The lower and upper bands (blue) have eigenstates delocalized in the bulk, whereas the states in the middle of the gap (green) are confined to the corners, as shown in **d**. The energy is expressed in units of λ. **d**, Theoretically calculated probability density functions (green circles; the areas of the circles correspond to the probability) of the four in-gap modes during reconfiguration of the lowest-edge unit cells from $\lambda_e/\gamma_e = 4.5$ (left) to $\lambda_e/\gamma_e = 1$ (centre) and to $\lambda_e/\gamma_e = 1/4.5$ (right). Throughout the deformation, only γ_e changes, while $\lambda_e = \lambda = 1$ and $\gamma = 1/4.5$. Experimental test results of this deformation are shown in Fig. 4.

[1]Department of Electrical and Computer Engineering, University of Illinois at Urbana-Champaign, Urbana, Illinois 61801-2918, USA. [2]Department of Physics, University of Illinois at Urbana-Champaign, Urbana, Illinois 61801-2918, USA. [3]Department of Mechanical Science and Engineering, University of Illinois at Urbana-Champaign, Urbana, Illinois 61801-2918, USA.

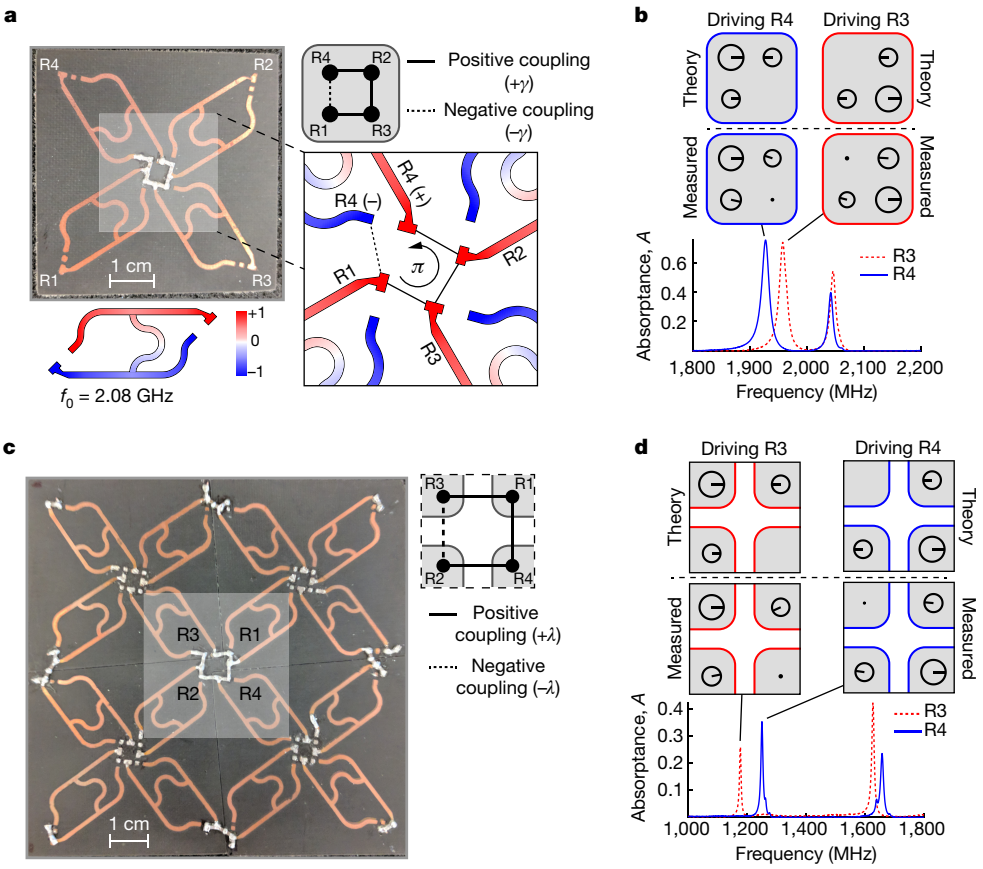

Figure 2 | Verification of microwave quadrupole lattice bulk topology. **a**, A unit cell of the quadrupole topological insulator (top left, photograph; top right, schematic) is composed of four H-shaped microstrip resonators that are capacitively coupled. Each resonator has a fundamental mode at $f_0 = 2.08$ GHz (colours represent normalized voltage amplitude; bottom left). The coupling between resonators R4 and R1 adds an extra phase shift of π (negative coupling), as shown in the detailed schematic (bottom right), to produce a π flux through the unit-cell plaquette. $\gamma \approx 35$ MHz. **b**, Eigenmode verification for the unit-cell plaquette. The resonator frequencies are shifted to about 2 GHz owing to capacitive loading from the coupling capacitors. The theoretical and measured eigenmodes are presented as phasor diagrams: the circle diameter corresponds to the magnitude of the resonator excitation, the line corresponds to the phase (0 is on the right and increases anticlockwise). When driving R4, R1 is in-phase, confirming the negative coupling between R1 and R4. **c**, A 2×2 test array of unit cells with $\gamma \to 0$. Negative coupling is set between R2 and R3, as illustrated in the schematic on the right. $\lambda \approx 150$ MHz. **d**, The eigenmodes of a plaquette formed by the four central resonators of a 2×2 array are similar to those of the unit cell because of the π flux. When driving R3, resonator R2 is in phase, confirming the negative coupling between these resonators. Here, the resonator frequencies are shifted to about 1.4 GHz owing to the greater capacitive loading than in the case of **b**.

non-trivial topology of the bulk, we focus on the latter, as these modes can provide direct spectroscopic evidence of the existence of the non-trivial quadrupole topological phase. Specifically, we experimentally demonstrate the existence of mid-gap modes that are localized at the corners of the lattice (Fig. 1d, left). Furthermore, we provide evidence that these corner modes are not due to surface effects, but are required by the topological bulk phase. We accomplish this by deforming one of the edges of the lattice from the topological to the trivial regime, and we observe that the mid-gap corner modes are not destroyed; instead, they recede into the sample, towards the corners on the newly generated boundaries of the quadrupole topological phase (Fig. 1d).

The microwave quadrupole topological insulator studied here consists of a square lattice of unit cells, in which each unit cell is composed of four identical resonators (Fig. 1b). The coupling rates γ and λ describe coupling between resonators within the same unit cell and between adjacent unit cells, respectively. Each plaquette, a square of any four adjacent resonators within or between unit cells, contains a single coupling term that carries an extra phase shift of π (dashed lines in Fig. 1b), which amounts to the generation of a synthetic magnetic π flux threading the plaquette (equivalent to half the magnetic flux quantum, $\frac{1}{2}\Phi_0 = h/(2e)$, where h is the Planck constant). The existence of this non-zero flux opens both the bulk and the edge spectral gaps, which are necessary to maintain the corner-localized mid-gap modes.

The resonators in our experimental array are H-shaped microstrip transmission lines that have a fundamental resonance at $f_0 = 2.08$ GHz, a typical linewidth of about 15 MHz and the spatial voltage distribution shown in Fig. 2a (bottom). At the centre of the cross-piece lies a voltage node and the end-points of the resonator are a quarter-wavelength away from the centre—they are therefore anti-nodes. Adjacent tips are separated by a half-wavelength and thus differ in phase by π. The resonators are designed so that anti-nodal points with opposite phases are physically close to each other, which facilitates the coupling of adjacent resonators with either no extra phase shift or an additional phase shift of π (negative coupling). To produce the quadrupole topology, in each plaquette we arrange three couplings as positive and one coupling as negative, as shown in Fig. 2a.

We experimentally confirm that a π flux threads each plaquette by examining the limiting cases of $\lambda \to 0$ and $\gamma \to 0$. This experimental verification is necessary to ensure that the spectral features that we measure are due to the bulk quadrupole topology, because corner modes—even topologically protected ones—are not unique to the quadrupole topological insulator[21,28,29]. In the $\lambda \to 0$ limit, the array consists of isolated unit-cell plaquettes, as shown in Fig. 2a. The behaviour of the array can be predicted theoretically by a direct diagonalization of the four-site Hamiltonian, a tight-binding representation of which is shown by the grey unit cell in Fig. 2a. For a coupling rate of γ between all resonators and a π flux threading the plaquette, the

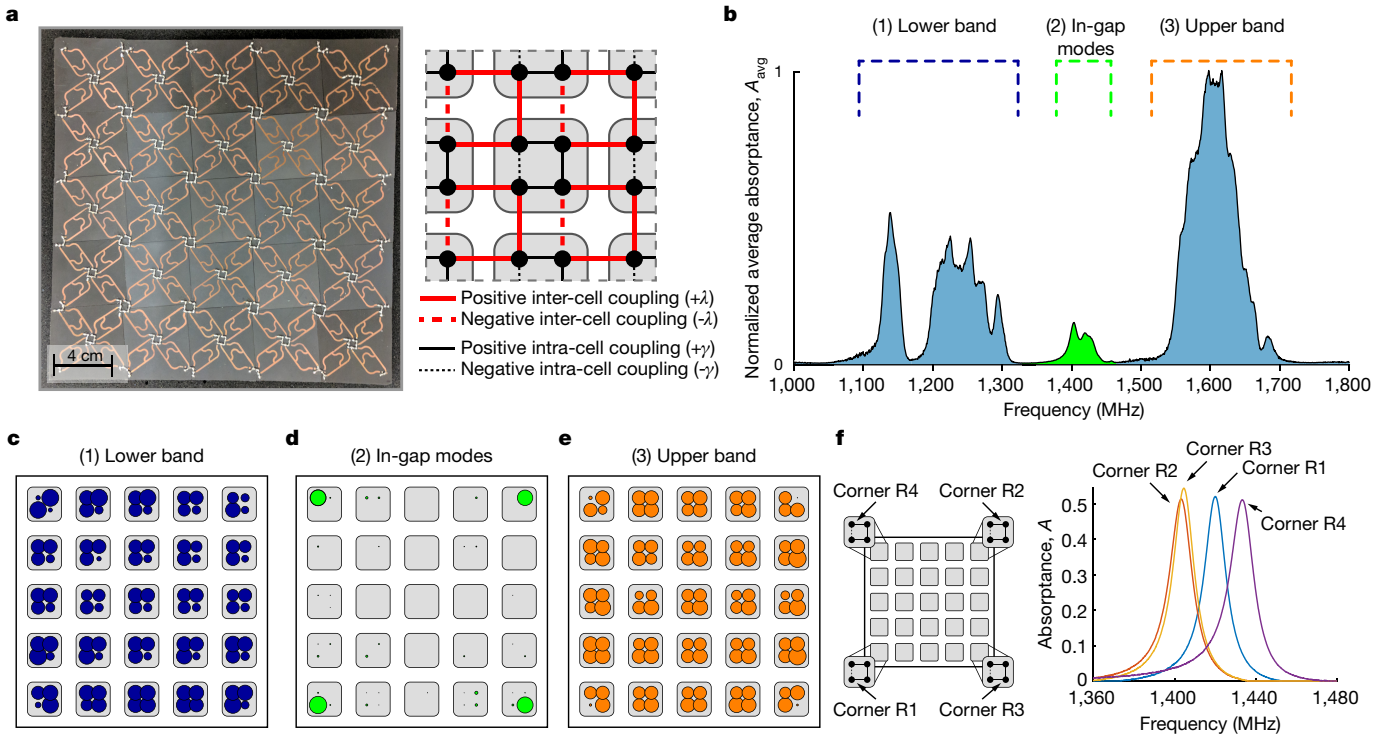

Figure 3 | Demonstration of microwave quadrupole topological insulator. a, Photograph of the experimental array of coupled resonators that form a quadrupole lattice. The array has 5×5 unit cells (Fig. 2a). We set the couplings to a ratio $\lambda/\gamma \approx 4.3$. The schematic on the right shows the connectivity of a bulk unit cell. **b**, Normalized average absorptance spectrum of all the resonators in the array (see Methods for details). We observe two large bands (blue) separated by a bandgap containing in-gap modes (green). **c**, Spatial distribution of absorptance summed over the lower frequency band indicated in **b**. Within this band, the response is dominated by bulk and edge resonators. The areas of the circles correspond to local absorptance. **d**, Spatial distribution of absorptance summed over the in-gap band noted in **b**. The in-gap modes are localized only on the corner resonators, which are not excited in the lower or upper band. **e**, Spatial distribution of absorptance summed over the upper band indicated in **b**, showing excitation of the bulk and edge resonators. **f**, Individual absorptance spectra of the corner resonators reveal that each corner resonator supports only a single mode.

eigenfrequencies are $\pm\sqrt{2}\,\gamma$, each of which is two-fold degenerate (see Methods). Because the non-trivial topology of the full array is clearly manifest in either the upper or the lower band (see Fig. 3b), we choose to characterize only the lower band, at $-\sqrt{2}\,\gamma$.

The measured power absorptance spectrum (the ratio of absorbed power to incident power) of an isolated unit cell is shown in Fig. 2b; see Methods for details on the measurement technique. As predicted by the Hamiltonian diagonalization, we find two pairs of nearly degenerate modes, separated by 88 MHz (measured on resonator R3) and 114 MHz (measured on R4). The discrepancy in mode frequency is due to asymmetric capacitive loading, which was present throughout our experiments (see Methods). The spatial distribution of the lower pair of modes is measured through the voltage amplitude and phase response at each resonator in the plaquette when either R3 or R4 is stimulated (see Methods). We find good agreement between the magnitudes and phases of the theoretical and measured modes (Fig. 2b): their normalized overlap integrals, calculated as an inner product of these modes, are about 0.98 and 0.97 when measured on R3 and R4, respectively. Characteristic mode shapes appear owing to destructive interference (caused by the π flux) between counter-circulating paths around the plaquette. Specifically, when R4 is excited, the mode vanishes for the diagonal resonator R3 (and vice versa). In Methods, we discuss the clear contrast of this situation with the modes predicted for plaquettes with zero flux, although the two cases can exhibit spectral similarities.

In the $\gamma \to 0$ limit, the array consists of isolated inter-unit-cell plaquettes (Fig. 2c, highlighted region). These plaquettes are nearly identical to the isolated unit cell, but the negative coupling is placed between R2 and R3 and the coupling rate λ is larger. We experimentally verify that the eigenmodes of this inter-unit-cell plaquette also have the features expected for a π flux by performing similar measurements to the single-unit-cell case (Fig. 2d). For this measurement, the capacitors that originally coupled the resonators within the unit cells are removed to ensure that $\gamma = 0$. Although the modes are again not perfectly degenerate, we find good agreement between the theoretical and measured mode shapes: their normalized overlap integrals are about 0.96 and 0.99 when measured on R3 and R4, respectively. The frequency separations of 450 MHz (measured on R3) and 408 MHz (measured on R4) between the two pairs of modes is on average about 4.3 times larger than in the isolated unit cell, revealing that the average ratio of the coupling rates is $\lambda/\gamma \approx 4.3$.

After the experimental verification of the plaquette building blocks, we construct a quadrupole topological insulator using a 5×5 array of unit cells (Fig. 3a) with coupling ratio $\lambda/\gamma \approx 4.3$ and the topology shown in Fig. 1b. The power absorptance spectrum of each resonator in the full array is measured in the same way as in the isolated plaquettes. The average absorptance across the entire array is presented in Fig. 3b. Three spectral bands are identifiable: broad lower and upper bands (blue) separated by a bandgap, and a narrow band of modes near the centre of the bandgap (green). The spatial distributions of these three bands, obtained by summing over each band, are shown in Fig. 3c–e. We find that, as predicted in ref. 11, modes in the lower and upper bands are predominantly localized on the bulk and edge resonators. The modes in the centre of the bandgap, which are associated with corner charges in the case of an electrical insulator, are highly localized on the corner resonators only. Despite the finite size of the array, the ratio of the coupling rates (λ/γ) is large enough that these corner modes decay rapidly and do not overlap with each other. In Fig. 3f, we show spectra measured within the bulk bandgap of the individual corner resonators, which reveal that each corner supports only a single mid-gap mode.

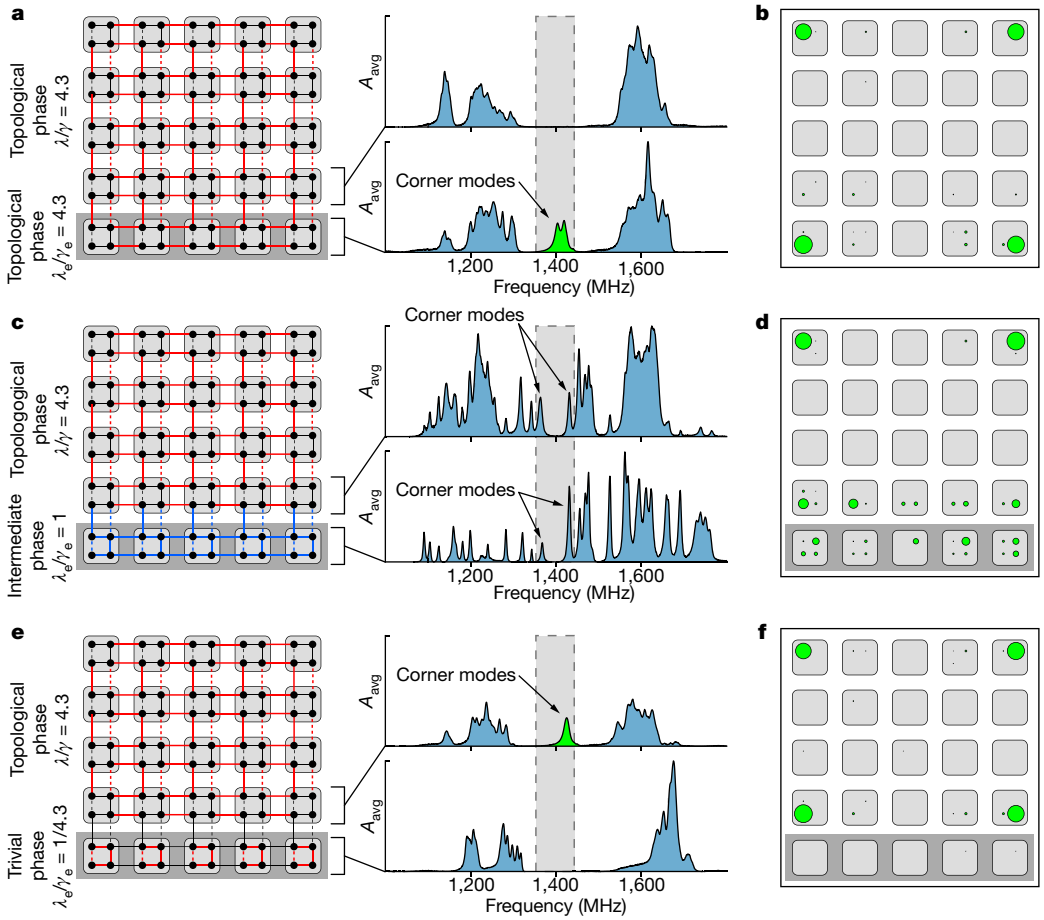

Figure 4 | Experimental test results for topologically protected corner states during edge deformation. a, The entire array is initially in the topological phase with $\lambda/\gamma = 4.3$. The bottom two rows of unit cells display a bandgap, with mid-gap modes—the topological corner modes—appearing only in the bottom row. **b**, Measured spatial distribution of modes within the bandgap, summed over the shaded band in **a**. **c**, The unit cells at the bottom edge are at a transition point between the topological and trivial regimes, with $\lambda_e/\gamma_e = 1$ (blue lines). The bandgap along the bottom edge narrows but remains open. Owing to the finite size of the array, the corner modes couple to each other and their degeneracy is lifted. **d**, Measured spatial distribution of modes within the bandgap, summed over the shaded band in **c**. The in-gap modes are delocalized between the unit cells in the bottom two rows. **e**, The unit cells in the bottom row are brought into the trivial regime, with $\lambda_e/\gamma_e = 1/4.3$, while the rest of the array remains topological. The mid-gap modes are shifted one row up, towards the new quadrupole topological phase boundary. **f**, Measured spatial distribution of the modes corresponding to the configuration shown in **e**. The mid-gap modes are confined to the new corners of the quadrupole topological phase.

As a consequence of the disorder in the array, which breaks the chiral and reflection symmetries, the measured spectrum is asymmetric with respect to its mid-gap point. Two main sources of disorder exist (see Methods for details): (i) systematic asymmetry in the coupling rates between resonators within the array, which arises from the physical implementation of negative coupling, and (ii) random manufacturing variations in the capacitance of the discrete coupling capacitors. The main spectroscopic effect of the asymmetric coupling rates is a splitting of the lower band, which manifests in isolated plaquettes as a lifting of the degeneracy of the lower pair of modes (Fig. 2). Despite the disorder and asymmetries, we find that the robust spectral features of the quadrupole topological insulator remain; for example, the spectral bands are gapped, with only four resonances close to the mid-gap position. Furthermore, we have verified that these four mid-gap modes are tightly confined to the corners (Fig. 3e).

To demonstrate that the corner-localized modes are not the result of local effects particular to the physical edges of the array, we tune the unit cells in the lowest row of the array from the topological regime ($\gamma < \lambda$) to the trivial regime ($\gamma > \lambda$). In this experiment, the entire array is initially in the original topological phase ($\lambda/\gamma \approx 4.3$), as shown in Fig. 3. For this configuration, we plot the average absorptance spectra of the bottom two rows of unit cells separately (Fig. 4a). The spectra reveal that both rows are gapped, but the bottom row supports the mid-gap modes, which are localized at the corners of the array (Fig. 4b). Next, we adjust the edge coupling rates in the bottom row of unit cells to be equal, that is, $\lambda_e/\gamma_e = 1$. This is achieved by changing the coupling capacitors within the network. This modification narrows the bandgap of the bottom two rows (Fig. 4c), and the two lower corner modes delocalize from the original corners into the surrounding unit cells (Fig. 4d). Owing to the finite size of the experimental array, the corner modes couple to each other at this point and their degeneracy is lifted. Finally, we make the bottom-edge unit cells trivial by setting $\lambda_e/\gamma_e \approx 1/4.3$, broadening the bandgap to its original width (Fig. 4e). Although the bottom edge of the array is now in the trivial regime, the corner modes are not destroyed, but recede to the new topological phase boundary. This experimental observation confirms that the corner modes are not a surface artefact, but are a manifestation of the bulk quadrupole topological phase. By contrast, if the corner modes were generated from local defects at the corners, or even if they arose as the end-states of edge-localized, one-dimensional topological dipole insulators, then the mid-gap modes would disappear during the edge deformation.

This work provides experimental evidence of a new family of topological phases of matter. Our metamaterial implementation of a quadrupole topological insulator confirms the existence of the theoretically predicted corner modes[11] and firmly establishes their origin from the

bulk quadrupole topology. This reconfigurable microwave platform can also readily support spatiotemporal modulation of both the resonance frequency and the coupling rates, enabling future experiments on dynamic topological phenomena, including pumping processes, quenches and chiral hinge modes[21]. In addition to the implementation described here, topological insulators with multipole moments could also be realized in photonic crystals, optical lattices of cold atoms[11] or crystalline materials[30], and parallel efforts have recently realized quadrupole topological insulators in electric and mechanical metamaterials[31,32]. The stage is set for rapid advances in topological physics at both the fundamental and device levels.

Online Content Methods, along with any additional Extended Data display items and Source Data, are available in the online version of the paper; references unique to these sections appear only in the online paper.

Received 8 October 2017; accepted 19 January 2018.

1. Zak, J. Berry's phase for energy bands in solids. *Phys. Rev. Lett.* **62,** 2747–2750 (1989).
2. Vanderbilt, D. & King-Smith, R. Electric polarization as a bulk quantity and its relation to surface charge. *Phys. Rev. B* **48,** 4442–4455 (1993).
3. Thouless, D., Kohmoto, M., Nightingale, M. & Den Nijs, M. Quantized Hall conductance in a two-dimensional periodic potential. *Phys. Rev. Lett.* **49,** 405–408 (1982).
4. Chang, C.-Z. *et al.* Experimental observation of the quantum anomalous Hall effect in a magnetic topological insulator. *Science* **340,** 167–170 (2013).
5. Kane, C. L. & Mele, E. J. Z_2 topological order and the quantum spin Hall effect. *Phys. Rev. Lett.* **95,** 146802 (2005).
6. Bernevig, B. A., Hughes, T. L. & Zhang, S.-C. Quantum spin Hall effect and topological phase transition in HgTe quantum wells. *Science* **314,** 1757–1761 (2006).
7. König, M. *et al.* Quantum spin Hall insulator state in HgTe quantum wells. *Science* **318,** 766–770 (2007).
8. King-Smith, R. D. & Vanderbilt, D. Theory of polarization of crystalline solids. *Phys. Rev. B* **47,** 1651–1654 (1993).
9. Thouless, D. J. Quantization of particle transport. *Phys. Rev. B* **27,** 6083–6087 (1983).
10. Fu, L. & Kane, C. L. Time reversal polarization and a Z_2 adiabatic spin pump. *Phys. Rev. B* **74,** 195312 (2006).
11. Benalcazar, W. A., Bernevig, B. A. & Hughes, T. L. Quantized electric multipole insulators. *Science* **357,** 61–66 (2017).
12. Su, W. P., Schrieffer, J. R. & Heeger, A. J. Solitons in polyacetylene. *Phys. Rev. Lett.* **42,** 1698–1701 (1979).
13. Hughes, T. L., Prodan, E. & Bernevig, B. A. Inversion-symmetric topological insulators. *Phys. Rev. B* **83,** 245132 (2011).
14. Turner, A. M., Pollmann, F. & Berg, E. Topological phases of one-dimensional fermions: an entanglement point of view. *Phys. Rev. B* **83,** 075102 (2011).
15. Leder, M. *et al.* Real-space imaging of a topologically protected edge state with ultracold atoms in an amplitude-chirped optical lattice. *Nat. Commun.* **7,** 13112 (2016).
16. Meier, E. J., An, F. A. & Gadway, B. Observation of the topological soliton state in the Su–Schrieffer–Heeger model. *Nat. Commun.* **7,** 13986 (2016).
17. Kraus, Y. E., Lahini, Y., Ringel, Z., Verbin, M. & Zilberberg, O. Topological states and adiabatic pumping in quasicrystals. *Phys. Rev. Lett.* **109,** 106402 (2012).
18. Slobozhanyuk, A. P., Poddubny, A. N., Miroshnichenko, A. E., Belov, P. A. & Kivshar, Y. S. Subwavelength topological edge states in optically resonant dielectric structures. *Phys. Rev. Lett.* **114,** 123901 (2015).
19. Blanco-Redondo, A. *et al.* Topological optical waveguiding in silicon and the transition between topological and trivial defect states. *Phys. Rev. Lett.* **116,** 163901 (2016).
20. Chaunsali, R., Kim, E., Thakkar, A., Kevrekidis, P. G. & Yang, J. Demonstrating an *in situ* topological band transition in cylindrical granular chains. *Phys. Rev. Lett.* **119,** 024301 (2017).
21. Benalcazar, W. A., Bernevig, B. A. & Hughes, T. L. Electric multipole moments, topological multipole moment pumping, and chiral hinge states in crystalline insulators. *Phys. Rev. B* **96,** 245115 (2017).
22. Wang, Z., Chong, Y., Joannopoulos, J. D. & Soljacic, M. Observation of unidirectional backscattering-immune topological electromagnetic states. *Nature* **461,** 772–775 (2009).
23. Hafezi, M., Mittal, S., Fan, J., Migdall, A. & Taylor, J. M. Imaging topological edge states in silicon photonics. *Nat. Photon.* **7,** 1001–1005 (2013).
24. Rechtsman, M. C. *et al.* Photonic Floquet topological insulators. *Nature* **496,** 196–200 (2013).
25. Nash, L. M. *et al.* Topological mechanics of gyroscopic metamaterials. *Proc. Natl Acad. Sci. USA* **112,** 14495–14500 (2015).
26. Susstrunk, R. & Huber, S. D. Observation of phononic helical edge states in a mechanical topological insulator. *Science* **349,** 47–50 (2015).
27. Ningyuan, J., Owens, C., Sommer, A., Schuster, D. & Simon, J. Time- and site-resolved dynamics in a topological circuit. *Phys. Rev. X* **5,** 021031 (2015).
28. Teo, J. C. & Hughes, T. L. Existence of Majorana-fermion bound states on disclinations and the classification of topological crystalline superconductors in two dimensions. *Phys. Rev. Lett.* **111,** 047006 (2013).
29. Benalcazar, W. A., Teo, J. C. & Hughes, T. L. Classification of two-dimensional topological crystalline superconductors and Majorana bound states at disclinations. *Phys. Rev. B* **89,** 224503 (2014).
30. Schindler, F. *et al.* Higher-order topological insulators. Preprint at https://arxiv.org/abs/1708.03636 (2017).
31. Imhof, S. *et al.* Topoelectrical circuit realization of topological corner modes. Preprint at https://arxiv.org/abs/1708.03647 (2017).
32. Serra-Garcia, M. *et al.* Observation of a phononic quadrupole topological insulator. *Nature* **555,** https://doi.org/10.1038/nature25156 (2018).

Acknowledgements We would like to thank J. T. Bernhard for access to the resources at the UIUC Electromagnetics Laboratory. This project was supported by the US National Science Foundation (NSF) through the Emerging Frontiers in Research and Innovation (EFRI) grant EFMA-1627184. C.W.P. acknowledges support from an NSF Graduate Research Fellowship. G.B. acknowledges support from the US Office of Naval Research (ONR) through a Director for Research Early Career Grant. W.A.B. and T.L.H. thank the US NSF for grant DMR-1351895.

Author Contributions C.W.P. designed the microwave quadrupole topological insulator, performed the microwave simulations and experimental measurements and produced the experimental figures. W.A.B. guided the topological insulator design and performed the theoretical calculations. T.L.H. and G.B. supervised all aspects of the project. All authors jointly wrote the paper.

Author Information Reprints and permissions information is available at www.nature.com/reprints. The authors declare no competing financial interests. Readers are welcome to comment on the online version of the paper. Publisher's note: Springer Nature remains neutral with regard to jurisdictional claims in published maps and institutional affiliations. Correspondence and requests for materials should be addressed to G.B. (bahl@illinois.edu).

Reviewer Information *Nature* thanks Y. Kivshar and the other anonymous reviewer(s) for their contribution to the peer review of this work.

METHODS

Spectrum and eigenmode measurements. We measure the power absorptance spectrum at each resonator in the tested networks by means of one-port reflection (S_{11}) measurements using a microwave network analyser (Keysight E5063A). The reflection probe is composed of a 50 Ω coaxial cable terminated in a 0.1 pF capacitor, which is connected to each resonator at an anti-node. Owing to the low probe capacitance, the measured linewidths are dominated by the intrinsic losses of each resonator.

The absorptance of each resonator is calculated as $A = 1 - |S_{11}|^2$. We also define the average absorptance for an array of N resonators as $A_{\mathrm{avg}} = \frac{1}{N}\sum_n^N A_n$, where A_n is the absorptance of the nth resonator. The average background absorptance contribution from the network analyser probe is evaluated far from any modes and removed during the measurements of A_n.

The eigenmodes of the unit cell and 2×2 array (Fig. 2) are also measured with a microwave network analyser by means of two-port transmission (S_{21}) measurements. The measurements are performed using a pair of probes with the specifications described above, with one probe providing the stimulus and the other measuring the response. Thus, the S_{21} transfer function at the resonance frequency represents a direct measurement of the amplitude and phase response of the corresponding eigenmode.

Design of the quadrupole topological insulator lattice. Each unit cell is fabricated individually on a Rogers RT/duroid 5880 substrate, with 35-μm-thick copper coating on each side. An approximate transmission line representation of our resonator is shown in Extended Data Fig. 1a. The resonator is H-shaped, with sections of approximately the same length (1.5 cm), width (0.1 cm) and characteristic impedance (about 110 Ω). This resonator design leads to an unloaded resonance frequency of 2.1 GHz in the transmission line model (the measured resonance frequency of a fabricated resonator is 2.08 GHz). Although there are losses in both the dielectric substrate and the copper conductor, as well as negligible radiative losses, these are small and do not affect the underlying topology.

To create a unit cell, four microstrip resonators are capacitively coupled as shown in Extended Data Fig. 1b. Each coupling is created using two 0.2 pF capacitors in series, resulting in a total coupling capacitance of 0.1 pF (related to the coupling parameter γ) between resonators within the unit cell. Negative coupling is realized by connecting R1 to the opposite-phase anti-node, R4.

The connections between unit cells are detailed in Extended Data Fig. 1c. Each capacitive coupling is formed using two 2 pF capacitors in series, resulting in a total inter-cell coupling capacitance (related to the coupling parameter λ) of 1 pF. The average coupling rates γ and λ are extracted from the measured data in the limits $\lambda \to 0$ and $\gamma \to 0$, respectively (Fig. 2). We find that the ratio of the frequency separations between the degenerate mode pairs in these isolated intra-unit-cell and inter-unit-cell cases is on average approximately 4.3, which implies a coupling rate ratio of $\lambda/\gamma \approx 4.3$.

Comparison of unit cells threaded with different fluxes. A unit cell of our quadrupole topological insulator is a square composed of four resonators threaded with π flux, as illustrated in Fig. 2a. In Fig. 2b, we show the measured eigenmodes of a single unit cell, which match well with the theoretically predicted modes. Here we discuss all four eigenmodes of this system and establish its differences from unit cells threaded with 0 flux. We find that without flux the modes differ substantially in their spatial distributions but their energy spectra can be similar if C_4 symmetry is broken.

The calculated energy spectrum and eigenmodes of a unit cell with π flux and equal coupling rates γ are shown in Extended Data Fig. 2a, along with a graphical representation of the Hamiltonian

$$H = \begin{pmatrix} 0 & 0 & \gamma & -\gamma \\ 0 & 0 & \gamma & \gamma \\ \gamma & \gamma & 0 & 0 \\ -\gamma & \gamma & 0 & 0 \end{pmatrix} \tag{1}$$

As noted in the main manuscript, there are two pairs of degenerate eigenmodes. These modes can be described by the orthonormal basis vectors

$$\begin{aligned} \boldsymbol{u}_1 &= \left(1/2 \;\; -1/2 \;\; 0 \;\; \sqrt{2}/2\right) \\ \boldsymbol{u}_2 &= \left(-1/2 \;\; -1/2 \;\; \sqrt{2}/2 \;\; 0\right) \\ \boldsymbol{u}_3 &= \left(-1/2 \;\; 1/2 \;\; 0 \;\; \sqrt{2}/2\right) \\ \boldsymbol{u}_4 &= \left(1/2 \;\; 1/2 \;\; \sqrt{2}/2 \;\; 0\right) \end{aligned} \tag{2}$$

where the elements of each vector are expressed relative to the complex amplitudes of the resonators R1, R2, R3 and R4. $\boldsymbol{u}_1$ and $\boldsymbol{u}_2$ represent the degenerate pair of lower-energy modes, and $\boldsymbol{u}_3$ and $\boldsymbol{u}_4$ describe the degenerate pair of higher-energy modes. In Fig. 2b we show the measurement results for modes $\boldsymbol{u}_1$ and $\boldsymbol{u}_2$. Owing to the destructive interference arising from the π flux within the plaquette, when one resonator is excited (here R3 or R4), the resonator in the opposite corner is not excited. This property leads to the characteristic modes of the unit cell. We also find that the location of the negative coupling affects the relative phase between the resonators, leading to the opposite relative phase between resonators with and without negative coupling.

We compare the above case with that of an identical unit cell with 0 flux, shown in Extended Data Fig. 2b and described by the Hamiltonian

$$H = \begin{pmatrix} 0 & 0 & \gamma & \gamma \\ 0 & 0 & \gamma & \gamma \\ \gamma & \gamma & 0 & 0 \\ \gamma & \gamma & 0 & 0 \end{pmatrix} \tag{3}$$

These modes can be described by the orthonormal basis vectors

$$\begin{aligned} \boldsymbol{v}_1 &= (1/2 \;\; 1/2 \;\; -1/2 \;\; -1/2) \\ \boldsymbol{v}_2 &= (0 \;\; 0 \;\; -\sqrt{2}/2 \;\; \sqrt{2}/2) \\ \boldsymbol{v}_3 &= (\sqrt{2}/2 \;\; -\sqrt{2}/2 \;\; 0 \;\; 0) \\ \boldsymbol{v}_4 &= (1/2 \;\; 1/2 \;\; 1/2 \;\; 1/2) \end{aligned} \tag{4}$$

In this unit cell, only modes $\boldsymbol{v}_2$ and $\boldsymbol{v}_3$ are degenerate, whereas $\boldsymbol{v}_1$ has lower energy and $\boldsymbol{v}_4$ has higher energy than $\boldsymbol{v}_2$ and $\boldsymbol{v}_3$. Because there is 0 flux threading the unit cell, when one resonator is excited, the resonator in the opposite corner is always excited as well.

Although a unit cell with 0 flux and identical horizontal and vertical coupling rates ($\gamma_x = \gamma_y$) is not gapped, a bandgap can be opened by setting $\gamma_x > \gamma_y$ (that is, by breaking C_4 symmetry). The energy spectrum and eigenmodes calculated for this case are shown in Extended Data Fig. 2c, along with a graphical representation of the Hamiltonian

$$H = \begin{pmatrix} 0 & 0 & \gamma_x & \gamma_y \\ 0 & 0 & \gamma_y & \gamma_x \\ \gamma_x & \gamma_y & 0 & 0 \\ \gamma_y & \gamma_x & 0 & 0 \end{pmatrix} \tag{5}$$

The modes can be described by the orthonormal basis vectors

$$\begin{aligned} \boldsymbol{w}_1 &= (1/2 \;\; 1/2 \;\; -1/2 \;\; -1/2) \\ \boldsymbol{w}_2 &= (1/2 \;\; -1/2 \;\; 1/2 \;\; -1/2) \\ \boldsymbol{w}_3 &= (1/2 \;\; -1/2 \;\; -1/2 \;\; 1/2) \\ \boldsymbol{w}_4 &= (1/2 \;\; 1/2 \;\; 1/2 \;\; 1/2) \end{aligned} \tag{6}$$

Although none of these modes is degenerate, the lower pair (and upper pair) can be brought arbitrarily close for a large ratio γ_x/γ_y. However, the spatial distribution of these eigenmodes clearly differs from that of a unit cell with π flux, since all four resonators are excited equally in each mode.

Systematic and random disorder caused by capacitive loading. The coupling capacitors also capacitively load the resonators, increasing their effective length and therefore reducing the resonance frequency. For bulk resonators, the capacitive loading is similar and does not affect the bulk spectral characteristics. However, the reduced capacitive loading for edge and corner resonators is compensated (to match the bulk loading) by adding a capacitance-to-ground of 0.6 pF and 1.2 pF to the edge and corner resonators, respectively. Small differences in the capacitive loading of the resonators inside our quadrupole topological insulator array imply disorder in both the resonance frequencies and the coupling rates.

The impact of this disorder is seen in the measured eigenmodes in the limits $\gamma \to 0$ and $\lambda \to 0$ (Fig. 2). In the full array, such disorder also results in splitting of the lower bulk band (Fig. 3b). To understand how these differences in capacitive loading arise, we examine two representative cases of resonators (Extended Data Fig. 3) loaded with identical total capacitance, but distinct spatial distributions.

In Extended Data Fig. 3a, we show the case where both capacitors are on the same arm of the resonator, as is the case for the intra-unit-cell coupling of resonators R1, R2 and R3 (Extended Data Fig. 1b) and the inter-unit-cell coupling of resonators R1, R2 and R4 (Extended Data Fig. 1c). The addition of a 2 pF capacitance-to-ground on one arm of the resonator causes a frequency shift to

1.4 GHz (compared with 2.1 GHz for the unloaded resonator). In Extended Data Fig. 3b, we examine the case where the same 2 pF capacitance is distributed to the two arms of the resonator, as is the case for the intra-unit-cell coupling of resonator R4 and for the inter-unit-cell coupling of resonator R3. Here, the resonance frequency shifts to 1.3 GHz; that is, it is lower than when both resonators are on the same arm. Although the total capacitance on each resonator is the same, these representative cases illustrate that the spatial distribution of capacitors affects the degree of capacitive loading on the resonator. Thus, systematic disorder in the capacitive loading of each resonator, which affects the coupling rate between resonators and their resonance frequencies, arises throughout our array.

In addition, the system exhibits random disorder due to variations in the manufacturing of its discrete components. Specifically, the 0.2 pF capacitors have a tolerance of ± 0.05 pF and the 2 pF capacitors have a tolerance of ± 0.1 pF. Despite this difference, the ratio λ/γ remains much larger than 1 throughout the array, so the bandgap remains open and the system remains firmly in the topological phase. A final source of disorder in the spectrum is the increase in the capacitive coupling rate with increasing frequency. Because of this effect, the lower bulk band is broader in frequency than the upper band.

Data availability. The data that support the findings of this study are available from the corresponding author on reasonable request.

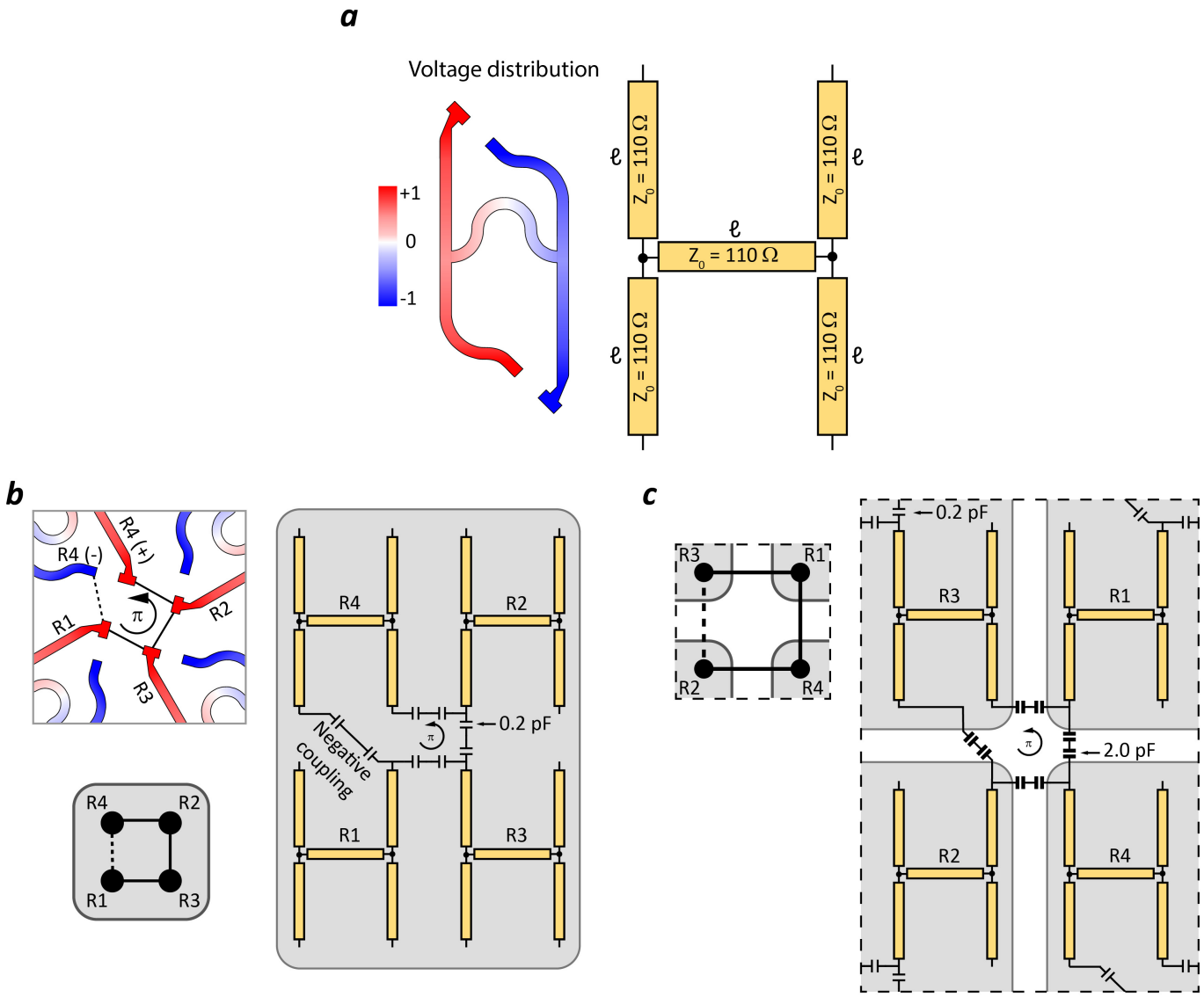

Extended Data Figure 1 | Transmission line model. a, Transmission line model of an individual microstrip resonator. Each section has approximately the same length $\ell = 1.5$cm and the same characteristic impedance $Z_0 = 110\ \Omega$, which give a fundamental resonance frequency of 2.1 GHz. **b**, Resonators coupled within the unit cell by two 0.2 pF capacitors in series. The capacitors linking R1 and R4 are connected to the out-of-phase anti-node of R4, creating π-flux threading in the plaquette. **c**, Coupling of resonators in different unit cells by two 2-pF capacitors in series. The capacitors between R2 and R3 are connected to the out-of-phase anti-node of R3 to produce the required π flux.

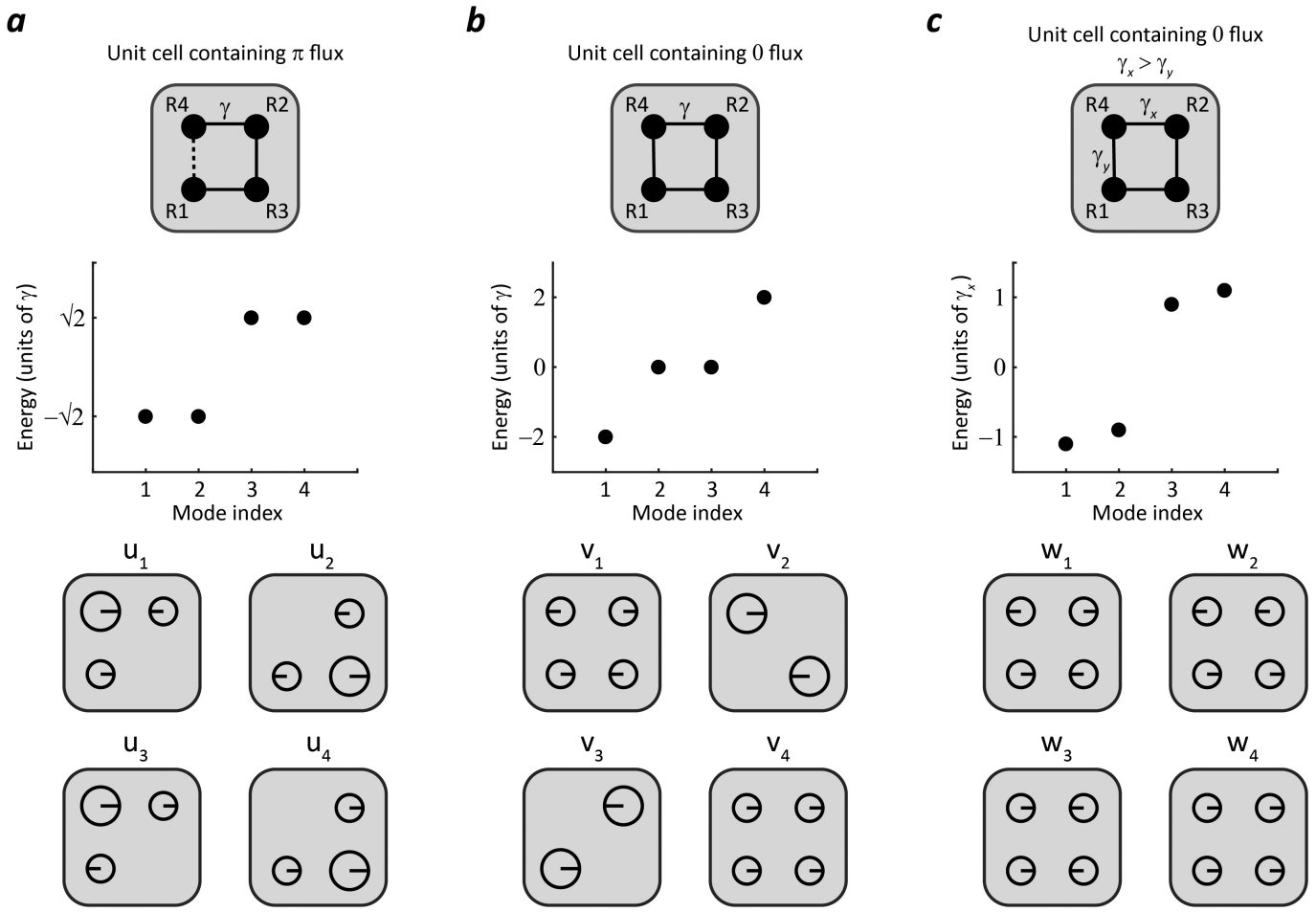

Extended Data Figure 2 | Comparison of unit cells threaded with π and 0 flux. a, Energy spectrum and eigenmodes of a unit cell with π flux. **b**, Energy spectrum and eigenmodes of a unit cell with 0 flux and $\gamma_x = \gamma_y$. **c**, Energy spectrum and eigenmodes of a unit cell with 0 flux and unequal coupling rates $\gamma_x > \gamma_y$. The energy separation between the lower two (and upper two) modes is proportional to γ_y.

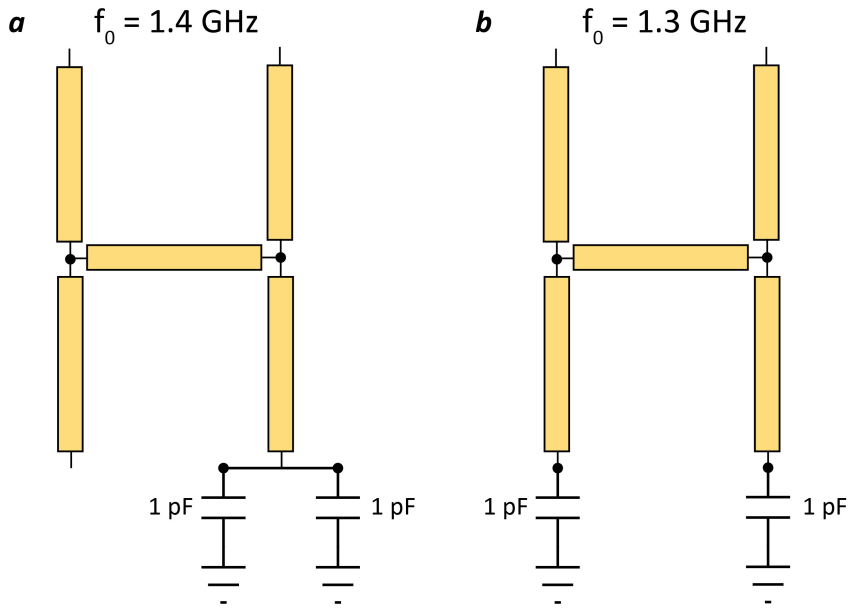

Extended Data Figure 3 | Comparison of resonators loaded with equal total capacitance. The resonance frequencies are calculated from simulations using Keysight ADS. **a**, A resonator with 2-pF loading on a single arm. The resonance frequency is shifted from 2.1 GHz to 1.4 GHz because of the loading. This situation corresponds to that of the intra-unit-cell coupling of resonators R1, R2 and R3 (Extended Data Fig. 1b) and the inter-unit-cell coupling of resonators R1, R2 and R4 (Extended Data Fig. 1c). **b**, A resonator with 2-pF loading distributed to two opposite-polarity arms. The resonance frequency is shifted from 2.1 GHz to 1.3 GHz owing to the loading. This situation is representative of the intra-unit-cell coupling of resonator R4 and the inter-unit-cell coupling of resonator R3.